# Morphology-Controlled Electrodeposition of Copper Gas Diffusion Electrodes for CO2 Electroreduction

Ismail, Ahmed Mohsen; Kortlever, Ruud

**DOI**
10.1021/acsaem.5c01142

**Publication date**
2025

**Document Version**
Final published version

**Published in**
ACS Applied Energy Materials

ACS APPLIED ENERGY MATERIALS



www.acsaem.org

Article

# Morphology-Controlled Electrodeposition of Copper Gas Diffusion Electrodes for $CO_2$ Electroreduction

Ahmed Mohsen Ismail and Ruud Kortlever*

Cite This: ACS Appl. Energy Mater. 2025, 8, 8551−8560

Read Online

ACCESS | Metrics & More | Article Recommendations | Supporting Information

**ABSTRACT:** Electrochemical carbon dioxide reduction ($CO_2R$) is an attractive route to use renewable electricity to convert $CO_2$ emissions to carbon-based chemicals. Continuous-flow electrolyzers with gas diffusion electrodes (GDEs) allow for the $CO_2R$ at high reaction rates. In addition to the electrolyzer configuration and operating conditions, the product selectivity strongly depends on the morphology of the electrocatalyst. This study demonstrates electrodeposition of copper (Cu) catalysts as a simple and efficient approach for preparing GDEs with good control over morphology. We study the influence of the activation process of the gas diffusion layer and the electrodeposition conditions on the morphology. Four Cu GDEs with different morphologies showed distinctly different current responses and product distributions. The partial current density for ethanol ($j_{ethanol}$) ranged from −18 mA $cm^{-2}$ to −29 mA $cm^{-2}$. Depending on the Cu GDE morphology, $j_{ethylene}$ ranged between −25 mA $cm^{-2}$ and −44 mA $cm^{-2}$. Although the catalyst layers revealed surface restructuring after $CO_2$ electrolysis, the morphologies remained distinctly different and retained the crystal structure of polycrystalline Cu. Electrodeposited Cu-GDEs maintained their selectivity for 6 h at a cell voltage of 4 V, representing a 5-fold improvement compared to sputtered Cu GDEs. Overall, this study demonstrates a facile approach for preparing GDEs with control over the catalyst morphology to tune $CO_2R$ to specific gaseous and liquid products.

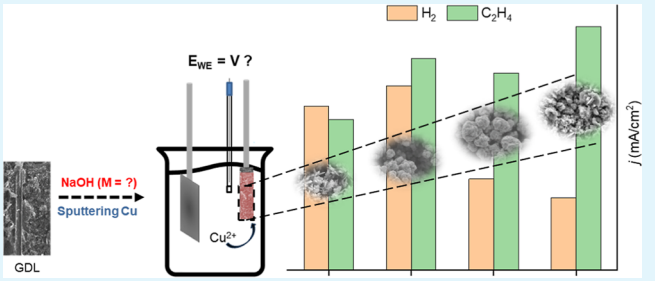


**KEYWORDS:** *carbon dioxide electrolysis, gas diffusion electrodes, electrodeposition, electrocatalysis, catalyst morphology*



## 1. INTRODUCTION

Fossil fuels and feedstocks still hold a leading position in today's energy matrix. The increasing $CO_2$ emissions in the atmosphere, the main cause of global climate change, have motivated the energy transition and sparked interest in the sustainable production of chemicals. Electrochemical technologies can play a pivotal role in addressing the challenges associated with the intermittent nature of renewable energy sources such as solar and wind. Among the various approaches available for $CO_2$ utilization, the electrochemical reduction of $CO_2$ to fuels and chemical feedstocks has gained considerable attention because of its mild operating conditions and is a promising route to close the carbon cycle powered by renewable electricity.[1−3] Moreover, electrochemical $CO_2$ reduction ($CO_2R$) presents a promising route to store renewable energy in the form of chemical bonds.[4]

$CO_2R$ is limited by its sluggish kinetics compared to the competing hydrogen evolution reaction (HER). Therefore, the development of electrocatalysts with good product selectivity, energy efficiency, and long-term stability is a key step toward application.[5−8] Much $CO_2R$ research has focused on the production of multicarbon ($C_{2+}$) products, such as ethylene ($C_2H_4$), ethanol ($C_2H_5OH$), and 1-propanol ($CH_3CH_2CH_2OH$), all of which hold significant promise as valuable chemical feedstocks and energy-rich fuels.[9−11] Among the various transition metals investigated, copper (Cu) uniquely exhibits a relatively high $C_{2+}$ product selectivity. This distinctive characteristic is attributed to its intermediate binding energy for carbon monoxide (CO), a key intermediate in the formation of products requiring more than two electron transfers.[12,13] However, the practical application of Cu electrocatalysts faces limitations due to poor selectivity toward one product, resulting in substantial downstream separation costs[14,15] and rapid catalyst deactivation, which favors the competing HER.[16] The deactivation of copper catalysts is often attributed to the detachment of catalytic particles[17] or morphology changes, induced by $CO_2R$ conditions such as local pH variations,[18] applied potentials,[19−21] and $CO_2R$ intermediates.[22] Some studies suggest that the reduction of copper oxides initiates cathodic dissolution. This process releases copper ions into the electrolyte, allowing for their

Received: April 17, 2025
Revised: May 29, 2025
Accepted: May 30, 2025
Published: June 4, 2025

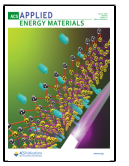

subsequent redeposition onto the electrode surface.[23,24] The unintended surface oxidation followed by anisotropic reduction results in the transformation of a smooth surface into a rough surface with more uncoordinated sites (the oxidation-induced morphological change mechanism).[25] These morphological alterations can occur upon polarization from the open circuit voltage (OCV),[20] as Cu electrodes are susceptible to oxidation at OCV potentials.[26] For example, a study reported by Velasco-Velez et al. showed that their electrodes exhibited a mixed-oxide composition of 40% metallic Cu and 60% $Cu_2O$ under the OCV conditions. During $CO_2R$, the electrode shrunk, indicating reduction due to oxygen loss from the copper oxide lattice.[27]

Consequently, numerous investigations have explored the impact of various parameters, including surface structure,[28] morphology,[29−31] composition,[32−34] and size[35] of Cu electrodes, on their electrocatalytic activity and selectivity. The specific surface structure significantly influences the electrocatalytic performance of copper during $CO_2$ reduction,[36] as different crystal facets of Cu exhibit varying selectivities toward specific products.[37] For instance, Cu (100) electrodes tend to favor C−C coupling, which is essential for the formation of $C_{2+}$ products, while the generation of oxygenates is preferred on both (100) and (110) facets.[15] Cubic Cu electrocatalysts, which are predominantly composed of (100) facets, have shown higher selectivity for $C_{2+}$ products compared to polycrystalline Cu.[30] 5-fold twinned Cu nanowires produced mainly methane ($CH_4$) with a faradaic efficiency (FE) of 55% at −1.25 V versus the reversible hydrogen electrode (RHE).[29] Cube-like structures, formed during electrolysis via structural transformations of Cu nanoparticle ensembles, selectively produced ethylene, ethanol, and 1-propanol.[38] Pulse electrodeposition yielded Cu electrodes with a rough surface morphology and a higher density of stepped facets compared with those formed by constant current electrodeposition. This increased the number of uncoordinated sites, resulting in a $CH_4$ FE of 85% at −2.8 V vs saturated calomel electrode (SCE).[31] The proportion of undercoordinated sites, which are often more reactive, can also be controlled by adjusting the size of the Cu catalyst. At a current density of 7.5 mA/cm$^2$, the $C_2H_4$ FE decreased from 92.8% to 83.4% when the Cu catalyst particle size range increased from 25 nm to 40−60 nm. Additionally, $C_2H_4$ was not detected with the 60−80 nm catalyst particles.[39] Furthermore, studies have demonstrated that transforming Cu nanocubes with predominantly (100) facets into a rhombic dodecahedral shape, characterized by high-energy (110) facets, resulted in a significant increase in the selectivity toward $C_{2+}$.[40] The strong correlation observed between the morphology of copper catalysts and the selectivity of $CO_2R$ products offers a critical avenue for optimizing catalyst design to preferentially produce desired multicarbon compounds.

Rational reactor design is crucial for enhancing the overall performance of the $CO_2R$. In comparison to traditional H-cells, flow cells have demonstrated the capability to enable the $CO_2R$ at significantly higher current densities. This improvement is primarily achieved by delivering $CO_2$ in the gas phase directly to the cathode, rather than relying on a $CO_2$-saturated electrolyte. This direct gas delivery method effectively overcomes the mass transport limitations that are inherent in H-cells due to the low solubility of $CO_2$ in aqueous electrolytes.[41−43] In these flow cells, the electrocatalysts are deposited onto a porous, gas-permeable gas diffusion layer (GDL) to form what is known as a gas diffusion electrode (GDE). GDLs commonly consist of a macroporous carbon fiber substrate (MPS) and a microporous layer (MPL) made of carbon black and polytetrafluoroethylene (PTFE). Alternatively, porous PTFE membranes are also employed as GDLs.[44]

Spray coating is currently the most prevalent technique employed for the preparation of GDEs. In this process, an ink containing the electrocatalyst particles and ionomers is deposited onto the GDLs.[45] However, this method necessitates the complete removal of any shape-directing agents, such as ligands, that were used during electrocatalyst synthesis. This step is critical to avoiding the blockage of active sites on the catalyst. Unfortunately, the process of removing these agents can often lead to the aggregation of the electrocatalyst particles during the preparation of the ink used for spray coating. Sputtering is an alternative method for fabricating Cu GDEs and has shown improvements in selectivity toward $C_{2+}$ products.[44,46] Nevertheless, sputtering typically results in the formation of spherical particles, which may not be optimal for all catalytic applications. Consequently, achieving precise control over the catalyst morphology within GDEs remains a significant challenge when using both spray coating and sputtering techniques.[15,44] Electrodeposition of Cu catalysts from aqueous solutions offers a potentially cost-effective strategy for preparing Cu GDEs with tailored morphologies and precise tuning of the amount of catalyst deposited.[47,48] However, this approach is not widely adopted for preparing Cu GDEs due to the hydrophobic nature of the GDLs. While pretreatment of GDLs with acid or base solutions can improve their wettability, the use of concentrated acid or base for activation can induce excessive hydrophilicity, which can compromise the gas diffusion properties of the GDL and lead to flooding of the GDE during $CO_2R$. Therefore, maintaining the essential hydrophobicity of the GDL while enabling sufficient wettability for electrodeposition remains a key challenge.[49−51] To overcome this challenge, alternative pretreatment methods that avoid the degradation of the GDL have been explored. These methods include the use of milder concentrations of acids and bases,[52] as well as coating the GDL with a thin layer of the target metal via physical deposition, such as sputtering.[50]

In previous work, copper films were electrodeposited using 3,5-diamino-1,2,4-triazole as an additive. By adjusting the pH and current density, the resulting morphology was controlled, yielding wire, dot, and amorphous structures. The Cu wire GDEs exhibited the best $CO_2R$ activity, achieving an FE of 40% for ethylene and 20% for ethanol at −0.5 V vs RHE.[49] This demonstrates the enhanced activity of nanosized porous Cu surfaces, which feature steps and edges of low-coordinated Cu atoms. These sites are more active and promote the adsorption and dimerization of $C_1$ intermediates. Furthermore, a lactic acid-derived $Cu_2O$ GDE prepared via electrodeposition exhibited $FE_{C2+}$ of 80% compared to a $FE_{C2+}$ = 60% of a spray-coated $Cu_2O$ nanocube electrode. This improved performance was attributed to its optimized surface area and higher density of grain boundaries and defects.[47] The in situ-electrodeposited Cu dendrites exhibited a significant decrease in ethylene selectivity at a current density of 170 mA/cm$^2$. The measurement was terminated after 150 min due to a rapid increase in the cell voltage. These results indicate the structural degradation of the initial active layer, characterized by localized sintering and oxidation. This degradation led to the loss of critical facets containing low-coordinated Cu atoms, which are


https://doi.org/10.1021/acsaem.5c01142
ACS Appl. Energy Mater. 2025, 8, 8551−8560

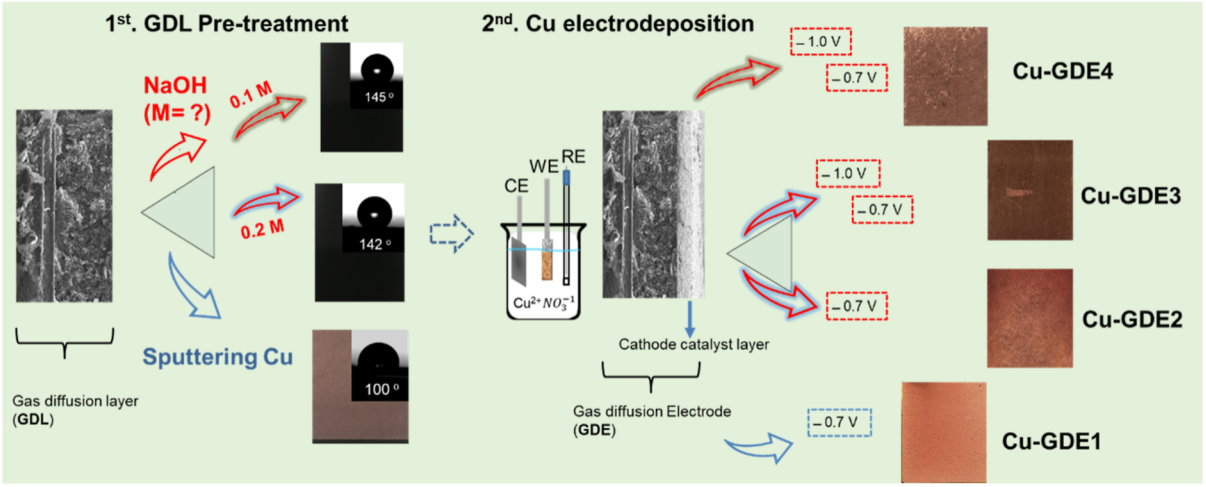


**Figure 1.** Preparation approach of Cu GDEs with different morphologies via electrodeposition. (WE: working electrode, CE: counter electrode, and RE: reference electrode).

essential for ethylene production.[16] Additionally, pretreatment of GDLs with water, sodium hydroxide, Triton X-100, and nitric acid has been shown to influence the subsequent electrodeposition of Cu, with nitric acid treatment resulting in the most homogeneously distributed Cu particles with high surface roughness. Increasing the nucleation potential resulted in a high density of smaller particles, while increasing the large growth potential (growth charge) led to larger particle sizes. Notably, Cu detachment was more prevalent in spray-coated GDEs than in electrodeposited Cu GDEs due to the lack of chemical bonding between the spray-coated Cu and the GDL.[52] Therefore, electrodeposition offers a viable alternative for preparing GDEs with controlled catalyst morphology and surface energy, leading to enhanced $CO_2R$ selectivity, activity, and durability. However, a systematic investigation of pretreatment approaches of GDLs and the optimization of electrodeposition conditions remains lacking.

Here, we present a facile and reproducible electrodeposition method for fabricating Cu GDEs with varying morphologies. This work demonstrates that activating GDLs with dilute NaOH does not induce detrimental hydrophilicity or electrolyte flooding during electrolysis. Furthermore, this study examines the impact of different GDL activation processes, including variations in NaOH concentration and the use of Cu sputtering, as well as the influence of electrodeposition conditions, on the resulting morphology of the catalyst layer. The $CO_2R$ performance of the prepared GDEs with different morphologies is evaluated using a hybrid electrolyzer with a 3 mm electrode separation. The results reveal significant differences in the electrocatalytic performance, depending on the GDL activation and electrodeposition methods employed. Notably, alkaline-activated GDLs activated with an alkaline solution yielded Cu GDEs that exhibited higher selectivity toward the formation of carbon monoxide, ethylene, and ethanol compared to Cu GDEs prepared using Cu-sputtered GDLs.

## 2. EXPERIMENTAL SECTION

**2.1. Materials.** All chemicals used in the GDL activation, electrode preparation, and electrolyte preparation were of analytical grade and were used without further purification. The following chemicals were used: sodium hydroxide (BioXtra ≥98% (acidimetric), pellets anhydrous, Sigma-Aldrich), copper(II) nitrate hemi(pentahydrate) (ACS reagent ≥99.99% Sigma-Aldrich), copper powder (<42 $\mu$m 99.5% Sigma-Aldrich), 2-propanol (Technical, VWR Chemicals), and potassium bicarbonate (≥99.95% Sigma-Aldrich). Milli-Q grade (Millipore Milli-Q IQ 7000) ultrapure deionized water was used for solution preparation. High-purity $CO_2$, $N_2$, Ar, He, and $H_2$ (99.999%, Linde) were used in the study.

**2.2. Electrode Preparation.** Cu GDEs with different morphologies (denoted here as Cu-GDE1, Cu-GDE2, Cu-GDE3, and Cu-GDE4) were prepared via the electrodeposition of copper catalysts on a carbon-based GDL (Sigracet 39BB, Fuel-Cell store). The electrodeposition experiments were carried out in a three-electrode, one-compartment cell using a Biologic SP-240 potentiostat. A platinum foil and a Ag/AgCl (3 M KCl, BASi MF-2056) electrode served as a counter electrode and a reference electrode, respectively. The distance between the working and counter electrodes was controlled to 2.5 cm. The GDLs were pretreated before the electrodeposition process to enable Cu deposition. Along with evaluating the impact of the pretreatment process on Cu electrodeposition, we studied one-step and two-step deposition methods to control Cu morphology through nucleation and growth rates. Cu was electrodeposited from a solution of 0.1 M $Cu(NO_3)_2$, with a cutoff charge of 9 C $cm^{-2}$ to control the Cu loading. A VCM 600 -SP3 Vacuum Thermal Evaporator Metalizer was employed to coat the GDL with a 40 nm copper film, operating at a current density of 80 A and a deposition rate of 0.5 Å/s under a vacuum ($1.5 \cdot 10^{-5}$ mbar). Further details on the preparation method of Cu GDEs are provided in the discussion in Figure 1 and Table S1.

After Cu electrodeposition, carbon nanotubes (CNTs) (MWCNTs, ACS materials) with a loading of 0.3 ± 0.1 mg $cm^{-2}$ were spray-coated on Cu GDEs preheated on a hot plate at 85 °C using a hand-held airbrush. The ink was prepared by dispersing CNTs powder in a solvent mixture of 1:1 water and isopropanol at a concentration of 5 mg $mL^{-1}$, containing 15 m/m % alkaline ionomer, Sustainion XA-9 (Dioxide Materials), based on the total mass of the catalyst and the ionomer combined. The CNT dispersion was homogenized in an ultrasonic bath for 20 min (the bath temperature was below 20 °C).

To prepare the anode, $IrO_2$ particles (Premion 99.99%, Alfa Aesar) were dispersed in a 1:1 water-isopropanol solvent mixture at a concentration of 20 mg $mL^{-1}$, containing 15 m/m % ionomer (Nafion 5 wt %, Sigma-Aldrich) with respect to the total mass of the catalyst and the ionomer. The dispersion was sonicated for 25 min in an ultrasonic bath (the bath temperature was kept below 20 °C). Then, the $IrO_2$ dispersion was spray-coated on a titanium screen (Fuel-Cell Store) preheated on a hot plate at 85 °C using a hand-held airbrush (Figure S1). The anode catalyst loading was 1.2 ± 0.1 mg $cm^{-2}$.

**2.3. Electrolyzer Tests.** All of the $CO_2R$ experiments were performed in a hybrid electrolyzer cell. We modified the zero-gap


https://doi.org/10.1021/acsaem.5c01142
ACS Appl. Energy Mater. 2025, 8, 8551−8560

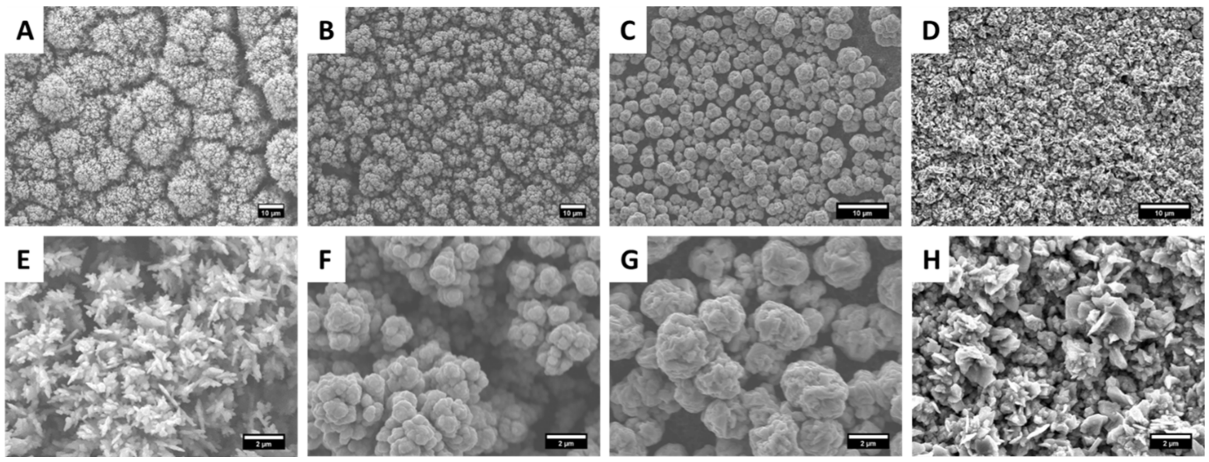


**Figure 2.** SEM images of the electrodeposited Cu GDEs. (A) Cu-GDE1, (B) Cu-GDE2, (C) Cu-GDE3, and (D) Cu-GDE4. (E–H) Corresponding high-magnification images.

configuration of a commercial membrane electrode assembly (MEA) $CO_2$ electrolyzer (Dioxide materials, T3 titanium anode current collector with a serpentine anolyte flow pattern and a S3 stainless steel cathode current collector with a serpentine flow pattern and an active area of 5 $cm^2$) by adding a catholyte flow field (Figure S2A,B) between the cathode GDE and the ion exchange membrane, while the anode catalyst was pressed directly to the membrane to assemble the cell in a hybrid configuration (Figure S2C). A Teflon catholyte flow field was designed with a thickness of 2.4 mm and sealed by two 0.3 mm Teflon gaskets, resulting in a 3 mm electrode spacing (Figure S2D). A cation exchange membrane (CEM, Nafion N117, Ion Power) was used to separate the cathode and anode compartments. The advantages of the hybrid configuration are as follows: (i) the flowing catholyte minimizes the direct effect of the membrane on the reaction conditions, as it serves as a buffer layer, determining the local chemical environment near the cathode catalyst layer (CCL) together with the electrode processes; (ii) a cation exchange membrane can be employed, as the conducted protons are shielded from the CCL by the liquid catholyte (1 M $KHCO_3$ was used in this work) and consumed in the local $CO_2$ regeneration via the conversion of bicarbonate back to $CO_2$ (Figure S3A); and (iii) a CEM blocks crossover of reactants, (bi)carbonate, and anionic products.

Electrolysis experiments with the hybrid $CO_2$ electrolyzer cell were carried out using the setup shown in Figure S3B. The gas-phase $CO_2$ feed rate was controlled by a mass flow controller (Bronkhorst F-201CV), and the cathode gas outlet flow rate was measured by a Bronkhorst F-101D-type mass flow meter. A 1 M $KHCO_3$ was used as the catholyte and anolyte and recirculated at a flow rate of 10 mL $min^{-1}$ using a peristaltic pump (Longer BT100-1L, Darwin microfluidics). The cathode gas-phase product mixture was collected in the headspace of the catholyte reservoir and then fed into the in-line sampling loop of gas chromatography (GC) every 10 min for quantification. The GC (Agilent 7890B) was equipped with a thermal conductivity detector (TCD) and a flame ionization detector (FID). A Molecular Sieve 3X column, SGE HT-8 0.25 $\mu$m capillary column, HayeSep Q packing (length 2.44 m) column, and HayeSep Q packing (length 0.5 m) column were used for the separation with argon as the carrier gas. To determine the volume fraction of gas products in the cathode outlet, we integrate the peaks and compare them to calibration curves generated from known concentrations of standard gases (Figures S4 and S5). The liquid samples from the catholyte and anolyte were collected at the end of electrolysis and analyzed using high-performance liquid chromatography (HPLC, Agilent 1260 Infinity). The liquid sample was injected onto two Aminex HPX-87H columns (Bio-Rad) connected in series and heated to a temperature of 60 °C. A 1 mM $H_2SO_4$ solution was used as the eluent, and a refractive index detector (RID) was used for the detection. Additionally, $^1$H NMR (Agilent DD2 400 spectrometer) was employed to quantify the liquid products using a solvent presaturation method to suppress the water signal. The liquid sample was mixed with phenol and dimethyl sulfoxide (DMSO) as an internal standard. Electrochemical measurements were performed using a Biologic SP-240 potentiostat equipped with a 4 A booster and electrochemical impedance spectroscopy. The measurements were run in a two-electrode setup. No *iR* correction was applied to the cell voltages reported throughout the manuscript.

**2.4. Electrode Characterization.** X-ray diffraction (XRD) measurements were conducted on a Bruker D8 advance diffractometer Bragg–Brentano geometry with a graphite monochromator and Vantec position sensitive detector, using Co k$\alpha$ radiation in the $2\theta$ range of 10°–110°, with a step size of 0.041° $2\theta$ and 1 s time per step. The $2\theta$ scale is converted to the Cu radiation scale. Scanning electron microscopy (SEM) images were collected using a JEOL JSM-6500F microscope operated at an accelerating voltage of 15 kV. Cross-section SEM images and energy dispersive X-ray spectroscopy (EDS) were employed using a JEOL IT800SHL field emission microscope operated at an accelerating voltage of 10 kV. Contact angle measurements were performed following GDL activation to assess the wetting properties. A 2 $\mu$L water droplet landed on the MPL. The droplet contour was analyzed from captured photographs using a CCD camera of a goniometer (OCA25, Dataphysics).

## 3. RESULTS AND DISCUSSION

**3.1. Preparation of Cu GDEs via Electrodeposition.** The fabrication of Cu GDEs in this study involved an electrodeposition technique, as schematically illustrated in Figure 1. Prior to electrodeposition, the MPL of the GDL underwent a pretreatment to facilitate the subsequent deposition of the copper catalyst. Two distinct pretreatment methods were employed: (i) immersion in dilute NaOH aqueous solutions for 24 h or (ii) sputtering of a thin Cu (40 nm for Cu-GDE1) onto the MPL via physical vapor deposition (SEM images and EDS of bare GDL and Cu-sputtered GDL are shown in Figures S6–S9). These pretreatment steps were implemented to modify the surface properties of the hydrophobic MPL, thereby enhancing the nucleation and adhesion of the electrodeposited Cu catalyst. Following both pretreatment methods, contact angle measurements were performed on the GDLs. The results indicated that, irrespective of the pretreatment, the contact angle remained ≥100°, confirming that the hydrophobic nature of the GDL was preserved, which is crucial for preventing electrolyte flooding during electrolysis. Then, the pretreated GDL was used as a substrate for Cu electrodeposition from a 0.1 M $Cu(NO_3)_2$ solution with a cutoff charge of 9 C $cm^{-2}$.



https://doi.org/10.1021/acsaem.5c01142
ACS Appl. Energy Mater. 2025, 8, 8551–8560

Additionally, one-step and two-step deposition methods were employed to tune the nucleation and growth rates, thereby controlling the morphology of the Cu structures. During electrodeposition, the backside of the GDL, the carbon fiber layer, was masked to keep its porous structure for the diffusion of $CO_2$ and gas-phase products and ensure Cu deposition only on the MPL. Table S1 summarizes all information regarding the preparation of each Cu-GDE, allowing for a direct comparison of the experimental conditions. Briefly, for Cu-GDE1, a GDL sputtered with 40 nm Cu was used as a substrate, and an electrodeposition potential of −0.7 V vs Ag/AgCl was applied. For Cu-GDE2 and Cu-GDE3, the pretreatment step involved using a 0.2 M NaOH solution. Subsequently, a one-step deposition at −0.7 V vs Ag/AgCl was applied for Cu-GDE2, while the Cu-GDE3 electrode was prepared using a two-step electrodeposition process. The first step involved applying a potential of −1.0 V vs Ag/AgCl with a cutoff charge of 0.2 C $cm^{-2}$, followed immediately by a second step at −0.7 V vs Ag/AgCl with a cutoff charge of 8.8 C $cm^{-2}$, resulting in a total deposited charge of 9 C $cm^{-2}$. Cu-GDE4 was prepared by activating the GDL in 0.1 M NaOH, followed by a two-step deposition: −1.0 V vs Ag/AgCl with a cutoff charge of 1 C $cm^{-2}$ and −0.7 V vs Ag/AgCl with a cutoff charge of 8 C $cm^{-2}$.

The XRD patterns of the electrodeposited Cu GDEs exhibited similar orientations (Figure S10), with diffraction peaks at $2\theta$ = 43.3, 50.5, and 74.2°, corresponding to the (111), (200), and (220) planes of the face-centered cubic (fcc) phase of Cu. SEM images of the bare GDL and 40 nm Cu-sputtered GDL are shown in Figure S6A,C. The sputtered Cu layer displayed spherical particle deposition. The morphologies of the prepared Cu GDEs are visualized using SEM (Figure 2). Cu-GDE1, electrodeposited at −0.7 V on a Cu-sputtered GDL, exhibited a flower-like structure composed of small flakes (Figure 2A,E). Activation with 0.2 M NaOH, followed by the same electrodeposition procedure, resulted in the formation of clusters with spherical structures (Cu-GDE2) (Figure 2B,F). Cu-GDE3, prepared via a two-step electrodeposition process (−1.0 V and −0.7 V), displayed cauliflower-like particles (Figure 2C,G), attributed to a nucleation step at −1.0 V followed by a slow growth process. A different two-step electrodeposition procedure was employed for the preparation of Cu-GDE4 (Figure 2D,H), using 0.1 M NaOH for GDL activation. The deposited catalyst exhibited interconnected flake growth. These results highlight the significant influence of the pretreatment step and the electrodeposition conditions on the overall catalyst morphology.

**3.2. Electrocatalytic Performance of Cu GDEs for $CO_2$R in a Hybrid Electrolyzer.** A schematic representation of the hybrid electrolyzer employed in this study is depicted in Figure S11. To enhance the hydrophobic properties of the electrodes, previous investigations have indicated that wrapping Cu wires with graphene oxide and utilizing PTFE as a surface modifier can effectively create hydrophobic electrodes and control the wettability of the catalyst layer.[29,53] In this study, we spray-coated CNTs onto the electrodeposited Cu GDEs to enhance the electrode hydrophobicity (Figure S12). Initially, we investigated the activity of the Cu-sputtered GDL. The Cu layer was added during the GDL pretreatment step, prior to the main Cu electrodeposition (Figure S13). The cell performance of this Cu-sputtered GDL was observed to be unstable, exhibiting a rapid loss of the selectivity toward $CO_2$R products, accompanied by a subsequent increase in the rate of HER. This suggests that the interface formed between the sputtered Cu and the GDL might not have been robust enough to sustain stable $CO_2$R. Further preliminary investigations involved evaluating the electrocatalytic performance of the CNTs. Figure S14 shows the electrocatalytic performance of the CNTs, which primarily generated CO and formate ($2e^-$ reduction products). The combined FE for these products was ∼9%, while the majority of the remaining charge was attributed to the HER. Therefore, CNTs do not possess significant intrinsic catalytic activity or selectivity for $CO_2$R and their primary role is to enhance the hydrophobicity of the main electrodes.

To determine the appropriate cell voltages for further investigations, linear sweep voltammetry (LSV) experiments were conducted on the different Cu GDEs. The purpose of these experiments, as depicted in Figure S15A, was to identify the cell voltages at which a current density of approximately −150 mA/$cm^2$ could be achieved. The voltammograms recorded for the different Cu GDEs in a 1 M $KHCO_3$ electrolyte revealed that there was no significant difference in the onset potentials. However, variations in the current responses became apparent at cell voltages of ≥3 V. These differences in current density are attributed to interruptions at the electrode−electrolyte interface caused by the evolution of gas bubbles. Notably, all four samples exhibited distinct current responses in this higher cell potential regime, indicating that the morphological differences between the Cu GDEs had a noticeable effect on their ability to handle higher reaction rates and the associated gas evolution. Consequently, based on these LSV results, three voltages (3.8, 4, and 4.2 V) were selected for the subsequent chronoamperometric experiments to thoroughly evaluate the impact of the electrode morphology on $CO_2$R performance and product selectivity under more controlled conditions.

The $CO_2$ feed rate affects the selectivity toward $C_{2+}$ products in $CO_2$R by altering the local pH at the catalyst layer.[54] A high $CO_2$ feed rate promotes a fast reaction with electrogenerated hydroxide ions near the catalyst layer, forming (bi)carbonate and consequently lowering the local pH. This lower pH environment generally favors the HER. Conversely, a low $CO_2$ feed rate will lead to mass transfer limitations, where the supply of $CO_2$ to the catalyst surface becomes insufficient, which can also enhance hydrogen evolution. To optimize this trade-off, we tested four $CO_2$ feed rates (20, 25, 30, and 35 sccm) at each of the three selected cell voltages. The $H_2$ FE reached a minimum of 19% at a $CO_2$ feed rate of 25 sccm and $E_{cell}$ = 4 V (Figure S16). Correspondingly, the FEs of the $CO_2$R products exhibited an opposite trend, suggesting that this feed rate provided a better balance between $CO_2$ availability and the local pH. A similar trend was observed at the other tested cell voltages (3.8 and 4.2 V). Based on these findings, a $CO_2$ feed rate of 25 sccm was selected for all subsequent experiments in this study.

The $CO_2$R performance of the electrodeposited Cu GDEs was evaluated under chronoamperometric conditions for a duration of 90 min. During these experiments, the FE of the gaseous products was quantified every 10 min, while the liquid products present in the catholyte were analyzed at the end of the electrolysis. The analysis of the products revealed that the four different Cu GDEs primarily generated carbon monoxide, ethylene, formate, ethanol, and 1-propanol as major products, whereas the remaining charge was mainly attributed to the HER. Minor products such as methane, acetate, and ethylene


https://doi.org/10.1021/acsaem.5c01142
ACS Appl. Energy Mater. 2025, 8, 8551−8560

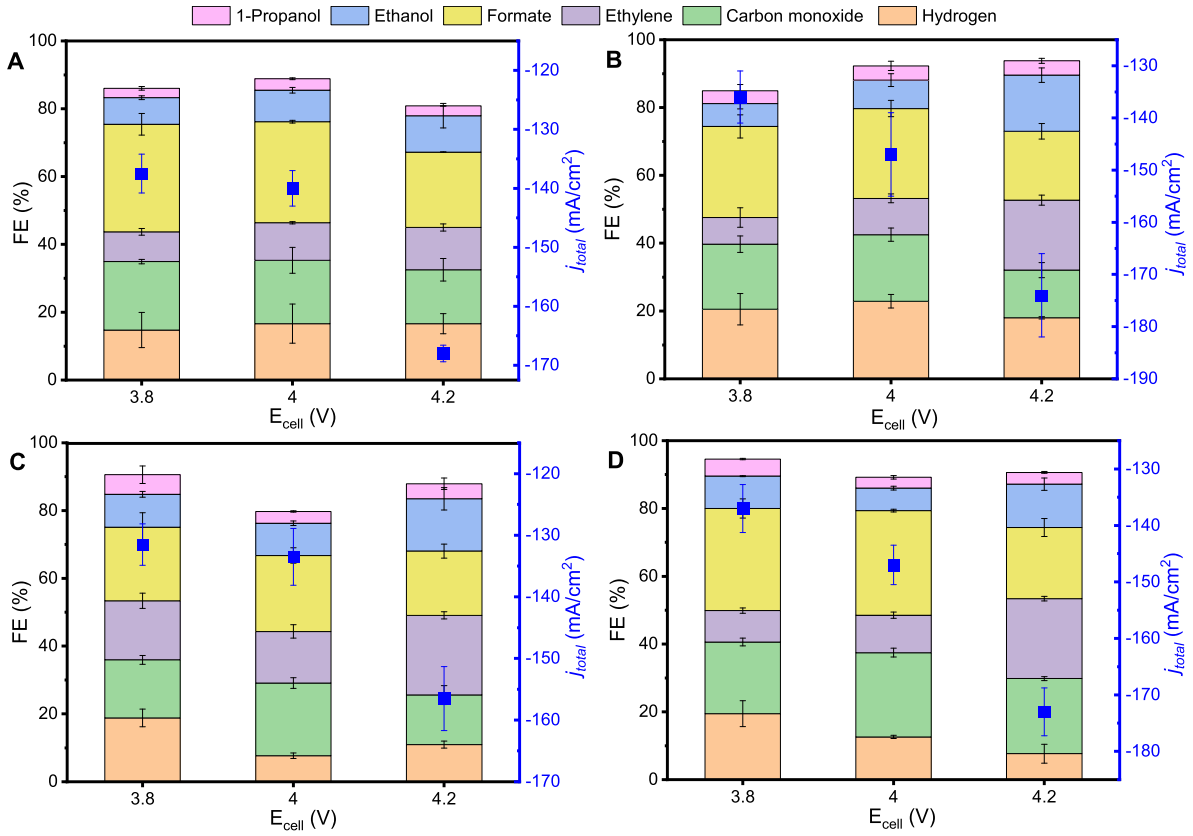


**Figure 3.** Electrochemical $CO_2$ reduction performance of Cu GDEs with different morphologies. Faradaic efficiency of the generated products and total current density as a function of a cell voltage, (A) Cu-GDE1, (B) Cu-GDE2, (C) Cu-GDE3, and (D) Cu-GDE4. Error bars represent the standard deviation over three samples.

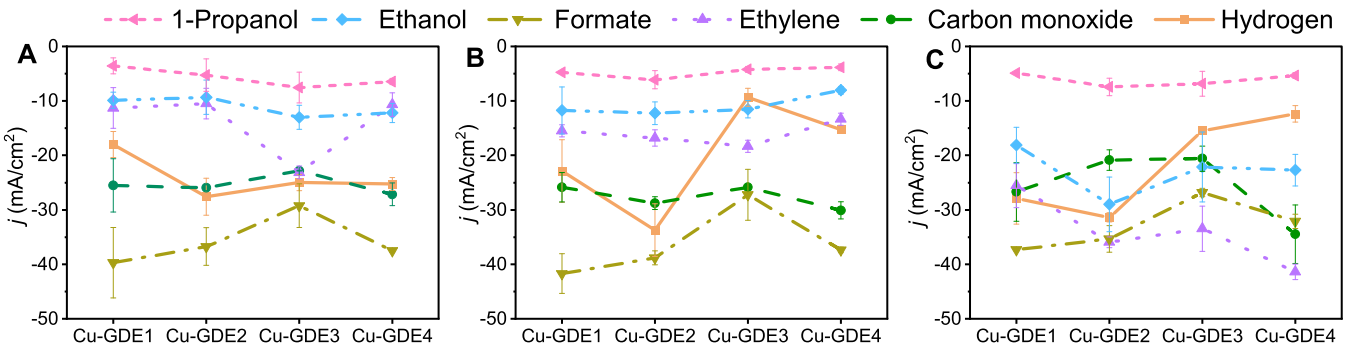


**Figure 4.** Electrochemical $CO_2$ reduction performance of Cu GDEs with different morphologies. Partial current density of the generated products at a cell voltage of (A) 3.8 V, (B) 4 V, and (C) 4.2 V. Error bars represent the standard deviation over three samples.

glycol were also detected with an FE $\leq$ 3% for all Cu GDEs. For the sake of simplicity and clarity, these minor products were not added to the figures. Figure S17 provides a comprehensive overview of all liquid products detected, including both major and minor components.

Figures S18–S21 present the chronoamperometric curves for the four Cu GDEs at the three tested cell voltages, along with the corresponding FE values and partial current densities for each product. Overall, the results demonstrate stable current densities and product distributions over the 90 min electrolysis at all tested voltages. The current density fluctuations are attributed to gas bubble formation at the electrode surface, which can block active sites, diffuse into the catholyte, alter the location of the triple-phase boundary, and potentially disturb local catholyte flow. The stable current density and product distribution imply that the GDL pores remained open for $CO_2$ gas diffusion to the catalyst layer, indicating no flooding.[55] This highlights the effectiveness of our system in mitigating the complex influence of pressure dynamics on the performance of a hybrid electrolyzer.[54] The total current density ($j_{total}$) at different voltages is shown in Figure 3. The $j_{total}$ was comparable at 3.8 and 4 V, but a significant increase was observed when the cell voltage was increased to 4.2 V. For example, the $j_{total}$ for Cu-GDE4 (Figure 3D) increased from −137 mA cm$^{-2}$ to −147 mA cm$^{-2}$ and −173 mA cm$^{-2}$ with increasing cell voltages. Comparing the performance of the different GDEs, we find that Cu-GDE2 and Cu-GDE4 exhibited comparable $j_{total}$ values at each of the applied voltages. Furthermore, both of these electrodes reached current densities higher than those of Cu-GDE1 and



https://doi.org/10.1021/acsaem.5c01142
ACS Appl. Energy Mater. 2025, 8, 8551−8560

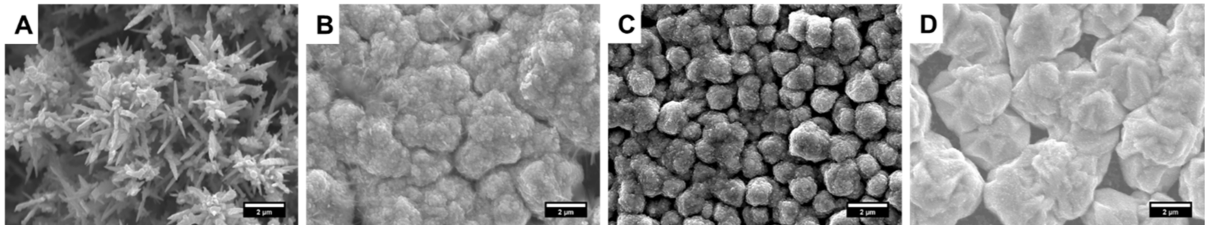


**Figure 5.** SEM images of the electrodeposited Cu-GDEs after electrolysis at 4.2 V for 90 min. (A) Cu-GDE1, (B) Cu-GDE2, (C) Cu-GDE3, and (D) Cu-GDE4.

Cu-GDE3. Specifically, at 4.2 V, the $j_{total}$ increased from −156 mA cm$^{-2}$ for Cu-GDE3 to −168 mA cm$^{-2}$ for Cu-GDE1, reaching −173 mA cm$^{-2}$ for both Cu-GDE2 and Cu-GDE4. This suggests that the morphology of Cu-GDE2 and Cu-GDE4 was more effective in promoting overall $CO_2$ reduction activity compared to Cu-GDE1 and Cu-GDE3.

To elucidate the influence of Cu electrodeposition conditions and the resulting morphology on catalytic activity toward $CO_2R$, we discuss the trends in FEs and partial current densities of the generated products. For Cu-GDEs prepared using alkaline pretreated GDLs (Cu-GDE2, Cu-GDE3, and Cu-GDE4), the FEs of ethylene, ethanol, and 1-propanol exhibited a clear dependence on the applied cell voltage. For instance, Cu-GDE4 showed an increase in the $FE_{C_2H_4}$ from 9% at 3.8 V to 24% at 4.2 V, whereas the $FE_{H2}$ decreased from 19% to 8%, and the $FE_{formate}$ decreased from 30% to 21%. Notably, the $FE_{CO}$ remained relatively constant at approximately 22%. This suggests that at 4.2 V, carbon monoxide production became more favorable over formate production, which can enhance C−C coupling when a sufficiently high surface coverage of carbon monoxide, a key intermediate for $C_{2+}$ products, is present. The $j_{H2}$ decreased from −25 mA cm$^{-2}$ to −10 mA cm$^{-2}$ for Cu-GDE3 and to −12 mA cm$^{-2}$ for Cu-GDE4 with increasing voltages, while Cu-GDE1 and Cu-GDE2 had similar HER rates across all applied voltages (Figure 4). This indicates that the two-step deposition process, used for Cu-GDE3 and Cu-GDE4, results in Cu structures with lower HER activity in comparison to the one-step Cu deposition method used for Cu-GDE1 and Cu-GDE2. At $E_{cell}$ = 3.8 V, the effect of morphology was less pronounced among Cu-GDE1, Cu-GDE2, and Cu-GDE4. These electrodes generated ethylene, ethanol, and carbon monoxide with partial current densities of about −10 mA cm$^{-2}$, −9 mA cm$^{-2}$, and −25 mA cm$^{-2}$, respectively (Figure 4A). However, Cu-GDE3, which has a cauliflower-like structure, exhibited an increase in the $j_{C_2H_4}$ to −23 mA cm$^{-2}$ and $j_{C_2H_5OH}$ to −13 mA cm$^{-2}$.

Figure 4B shows that the activity patterns at 4 V are comparable to those at 3.8 V, with diminished HER activity. At $E_{cell}$ = 4.2 V, a clear morphology dependence was observed (Figure 4C). Cu-GDE1, featuring a flower-like structure, exhibited a $j_{CO}$ of −27 mA cm$^{-2}$. The $j_{CO}$ of Cu-GDE2 and Cu-GDE3 decreased to −21 mA cm$^{-2}$, while Cu-GDE4 showed an increase to −34 mA cm$^{-2}$. The $j_{formate}$ followed a volcano-like trend, decreasing from −37 mA cm$^{-2}$ to −27 mA cm$^{-2}$ and then increasing to −32 mA cm$^{-2}$ over Cu-GDE4. Cu-GDE4, characterized by an interconnected nanoflake structure, exhibited the highest $j_{C_2H_4}$ of −44 mA cm$^{-2}$. The $j_{C_2H_5OH}$ peak of −29 mA cm$^{-2}$ was achieved for Cu-GDE2, which comprises structured clusters of spherical particles. Overall, the Cu-GDEs prepared from alkaline-activated GDLs demonstrated higher selectivity toward carbon monoxide, ethylene, and ethanol compared to Cu GDEs prepared from Cu-sputtered GDLs (method used for Cu-GDE1).

After electrolysis, the XRD patterns of the Cu-GDEs revealed reflections at positions consistent with the fcc phase of Cu, mirroring the as-prepared Cu-GDE (Figure S23). However, the intensity of these peaks increased, and the peaks broadened, indicating surface restructuring toward a rough surface with more uncoordinated sites, such as steps and kinks.[31,56]

Furthermore, reflections corresponding to the $Cu_2O$ phase were also present. This is attributed to the spontaneous oxidation of Cu catalysts after electrolysis, as the catalyst layer was exposed to the catholyte, and the reduction potential was no longer applied. Figure 5 illustrates the post-electrolysis morphology of the electrodeposited Cu catalysts. We observe morphological changes, while the morphology of the Cu-GDEs remained distinctly different after electrolysis. This implies that the initial morphology plays a role in how the catalyst restructures during electrolysis. In Cu-GDE1, the initial flakes partially restructured into needle-like structures. Larger aggregates are formed in Cu-GDE2 and Cu-GDE3, consisting of very small particles assembled into regular patterns, preserving the shape of the initially electrodeposited Cu catalysts. Cu-GDE4 exhibited coalescence of the nanoflakes into larger entities (Figure 5D). The morphological changes observed under reaction conditions reveal the tendency of Cu for surface reconstruction.[19] Furthermore, nanoclustering followed by coalescence driven by the applied negative potential has been proposed as the degradation pathway.[57]

The stability of the electrodeposited Cu-GDEs in a hybrid electrolyzer with a cation exchange membrane was investigated at a cell voltage of 4 V. The four different Cu-GDEs exhibited a stable current density of approximately 130 mA/cm$^2$ (see Figure S24). After 3 h, Cu-GDE3 exhibited a shift in selectivity from $CO_2R$ to HER, attributed to morphological changes and the formation of nanoparticle clusters (see Figure 5C). This observation aligns with a previous report indicating that nanoclusters with a higher population of low-coordinated sites favor HER and that nanoclustering (the first stage of the degradation pathway) is primarily induced by the applied potential.[57] Cu-GDE2 and Cu-GDE4 maintained their performance for 6 h. The formation of large aggregates (Figure 5B,D) resulted in a decrease in HER, likely due to a reduction in the number of low-coordinated sites through nanoclustering and coalescence. Besides the initial flakes, the formation of needle-like clusters was observed on Cu-GDE1 after 8 h of electrolysis (Figure S25). The $H_2$ FE gradually increased from 18% to 30%, while the FEs of carbon monoxide, ethylene, and ethanol decreased to 12%, 6%, and 6%, respectively. Catalyst reduction and oxygen loss from the oxide lattice, along with


https://doi.org/10.1021/acsaem.5c01142
ACS Appl. Energy Mater. 2025, 8, 8551−8560

detachment/redeposition of particles, affect the surface metal loading, leading to different activities among the Cu-GDEs.[19,20,22] The evolution of large aggregates was associated with greater CO production and improved the selectivity toward ethanol on Cu-GDE2 and ethylene on Cu-GDE4.

Notably, Cu-GDE2 and Cu-GDE4 maintained their performance, including selectivity toward $CO_2$ reduction products, representing a 5-fold improvement in operational lifetime compared to GDEs prepared by sputtering in a hybrid electrolyzer system utilizing the same electrolyte and electrode area.[54] Moreover, with this hybrid configuration, we achieved a current density of −175 mA/cm$^2$ at a cell voltage of 4.2 V, significantly outperforming a previously reported system (~5.5 V at 150 mA/cm$^2$) with unstable performance. Electrodeposition is a technique that can be readily scaled up for the production of large-area electrodes with robust catalyst attachment, which is crucial for industrial applications.

## 4. CONCLUSIONS

We report a straightforward electrodeposition strategy successfully employed to synthesize four distinct Cu GDEs (Cu-GDE1, Cu-GDE2, Cu-GDE3, and Cu-GDE4). This method involved a two-step process: first, GDL activation via either alkaline treatment or Cu sputtering; second, Cu electrodeposition from a 0.1 M $Cu(NO_3)_2$ solution at a controlled deposition potential. By carefully adjusting the GDL pretreatment and the electrodeposition conditions, we achieved a variety of Cu catalyst morphologies. The performance of these Cu GDEs in $CO_2R$ was evaluated in a hybrid electrolyzer under chronoamperometric conditions at three different cell voltages (3.8, 4, and 4.2 V) to determine the impact of catalyst morphology on product selectivity and partial current density. The primary products observed were carbon monoxide, ethylene, formate, ethanol, and 1-propanol, whereas the remaining charge was mainly attributed to the HER. Notably, Cu-GDE4, characterized by an interconnected flake structure, exhibited a $j_{total}$ of −173 mA cm$^{-2}$ at 4.2 V. Cu-GDE2 and Cu-GDE4 exhibited comparable and higher $j_{total}$ values than Cu-GDE1 and Cu-GDE3. Morphological changes were observed, and the morphology of the Cu-GDEs remained distinctly different after electrolysis. This implies that the starting morphology plays a role in how the catalyst restructures during electrolysis. Cu-GDE3 exhibited a shift in the selectivity from $CO_2R$ to HER, attributed to morphological changes and the formation of nanoparticle clusters. The formation of larger aggregates led to increased CO production and, consequently, higher selectivity for ethanol with Cu-GDE2 and for ethylene with Cu-GDE4. We observed the development of needle-like clusters on the Cu-GDE1 electrode after 8 h of electrolysis. During this time, the $H_2$ FE progressively increased from 18% to 30%, while the FEs of carbon monoxide, ethylene, and ethanol declined to 12%, 6%, and 6%, respectively.

Overall, our findings indicate that alkaline-activated GDLs led to Cu GDEs with enhanced selectivity for CO, $C_2H_4$, and $C_2H_5OH$ compared to Cu GDE1, which was prepared from a Cu-sputtered GDL. Furthermore, we observed that employing a two-step deposition process effectively suppressed the HER. X-ray diffraction (XRD) patterns confirmed that the polycrystalline nature of the copper catalysts was maintained, although with increased peak intensity and width, suggesting surface restructuring under reaction conditions. During a 6 h experiment at a cell voltage of 4 V, Cu-GDEs maintained a stable current density of approximately 120 mA/cm$^2$, with Cu-GDE2 and Cu-GDE4 retaining their selectivity toward $CO_2$ reduction products, demonstrating a 5-fold improvement in operational lifetime compared to GDEs prepared by sputtering in a similar hybrid system.[54] The enhanced performance and stability observed with specific electrodeposited copper morphologies on alkaline-activated GDLs highlight the potential of this approach for advancing the field of electrochemical $CO_2$ reduction toward practical industrial applications.

## ■ ASSOCIATED CONTENT

### Supporting Information

The Supporting Information is available free of charge at https://pubs.acs.org/doi/10.1021/acsaem.5c01142.

Photographs of the hybrid electrolyzer and schematic piping and instrumentation diagram of the test framework; XRD spectra; SEM images; EDS mapping; LSV curves; chronoamperometric curves and Faradaic efficiencies; $^1$H NMR spectra; and electrolyte pH and conductivity (PDF)

## ■ AUTHOR INFORMATION


### Corresponding Author

**Ruud Kortlever** − *Large-Scale Energy Storage Section, Department of Process & Energy, Faculty of Mechanical Engineering, Delft University of Technology, Delft 2628 CB, The Netherlands;* orcid.org/0000-0001-9412-7480; Email: r.kortlever@tudelft.nl

### Author

**Ahmed Mohsen Ismail** − *Large-Scale Energy Storage Section, Department of Process & Energy, Faculty of Mechanical Engineering, Delft University of Technology, Delft 2628 CB, The Netherlands; Department of Chemistry, Faculty of Science, Alexandria University, Alexandria 21511, Egypt;* orcid.org/0000-0002-6899-3577

Complete contact information is available at: https://pubs.acs.org/10.1021/acsaem.5c01142


### Author Contributions

A.M.I. carried out the experimental work, analyzed the results, and wrote the manuscript. R.K. analyzed the results and edited and supervised the work.

### Notes

The authors declare no competing financial interest.

## ■ ACKNOWLEDGMENTS

This project received funding from the NWO-AES Crossover program under project number 17621 (RELEASE). The authors acknowledge Ruud Hendrikx for the X-ray diffraction analysis and Michel van den Brink for lab management and organizing the work environment.

## ■ REFERENCES

(1) De Luna, P.; Hahn, C.; Higgins, D.; Jaffer, S. A.; Jaramillo, T. F.; Sargent, E. H. What Would It Take for Renewably Powered Electrosynthesis to Displace Petrochemical Processes? *Science* **2019**, *364* (6438), 3506.

(2) Bushuyev, O. S.; De Luna, P.; Dinh, C. T.; Tao, L.; Saur, G.; van de Lagemaat, J.; Kelley, S. O.; Sargent, E. H. What Should We Make with $CO_2$ and How Can We Make It? *Joule* **2018**, *2* (5), 825−832.

(3) Whipple, D. T.; Kenis, P. J. A. Prospects of $CO_2$ Utilization via Direct Heterogeneous Electrochemical Reduction. *J. Phys. Chem. Lett.* **2010**, *1* (24), 3451−3458.
(4) Weekes, D. M.; Salvatore, D. A.; Reyes, A.; Huang, A.; Berlinguette, C. P. Electrolytic $CO_2$ Reduction in a Flow Cell. *Acc. Chem. Res.* **2018**, *51* (4), 910−918.
(5) Kumar, B.; Brian, J. P.; Atla, V.; Kumari, S.; Bertram, K. A.; White, R. T.; Spurgeon, J. M. New Trends in the Development of Heterogeneous Catalysts for Electrochemical $CO_2$ Reduction. *Catal. Today* **2016**, *270*, 19−30.
(6) Kortlever, R.; Shen, J.; Schouten, K. J. P.; Calle-Vallejo, F.; Koper, M. T. M. Catalysts and Reaction Pathways for the Electrochemical Reduction of Carbon Dioxide. *J. Phys. Chem. Lett.* **2015**, *6* (20), 4073−4082.
(7) Lin, Z.; Han, C.; O'Connell, G. E. P.; Lu, X. Recent Progress on Electrode Design for Efficient Electrochemical Valorisation of $CO_2$, $O_2$, and $N_2$. *Angew. Chem., Int. Ed.* **2023**, *62*, 202301435.
(8) Ross, M. B.; De Luna, P.; Li, Y.; Dinh, C.-T.; Kim, D.; Yang, P.; Sargent, E. H. Designing Materials for Electrochemical Carbon Dioxide Recycling. *Nat. Catal.* **2019**, *2* (8), 648−658.
(9) Lawrence, K. R.; Kumar, A. S.; Asperti, S.; van den Berg, D.; Girichandran, N.; Kortlever, R. Advances in Electrochemical Carbon Dioxide Reduction Toward Multi-Carbon Products. In *Chemical Valorisation of Carbon Dioxide*; Stefanidis, G., Stankiewicz, A., Eds.; The Royal Society of Chemistry, 2022; pp 388−412..
(10) Li, Y. C.; Wang, Z.; Yuan, T.; Nam, D. H.; Luo, M.; Wicks, J.; Chen, B.; Li, J.; Li, F.; De Arquer, F. P. G.; Wang, Y.; Dinh, C. T.; Voznyy, O.; Sinton, D.; Sargent, E. H. Binding Site Diversity Promotes $CO_2$ Electroreduction to Ethanol. *J. Am. Chem. Soc.* **2019**, *141* (21), 8584−8591.
(11) Kuhn, A. N.; Zhao, H.; Nwabara, U. O.; Lu, X.; Liu, M.; Pan, Y. T.; Zhu, W.; Kenis, P. J. A.; Yang, H. Engineering Silver-Enriched Copper Core-Shell Electrocatalysts to Enhance the Production of Ethylene and $C_{2+}$ Chemicals from Carbon Dioxide at Low Cell Potentials. *Adv. Funct. Mater.* **2021**, *31* (26), 2101668.
(12) Bagger, A.; Ju, W.; Varela, A. S.; Strasser, P.; Rossmeisl, J. Electrochemical $CO_2$ Reduction: A Classification Problem. *ChemPhysChem* **2017**, *18* (22), 3266−3273.
(13) Hori, Y.; Murata, A.; Takahashi, R. Formation of Hydrocarbons in the Electrochemical Reduction of Carbon Dioxide at a Copper Electrode in Aqueous Solution. *J. Chem. Soc., Faraday Trans. 1* **1989**, *85* (8), 2309.
(14) Kuhl, K. P.; Cave, E. R.; Abram, D. N.; Jaramillo, T. F. New Insights into the Electrochemical Reduction of Carbon Dioxide on Metallic Copper Surfaces. *Energy Environ. Sci.* **2012**, *5* (5), 7050.
(15) Nitopi, S.; Bertheussen, E.; Scott, S. B.; Liu, X.; Engstfeld, A. K.; Horch, S.; Seger, B.; Stephens, I. E. L.; Chan, K.; Hahn, C.; Nørskov, J. K.; Jaramillo, T. F.; Chorkendorff, I. Progress and Perspectives of Electrochemical $CO_2$ Reduction on Copper in Aqueous Electrolyte. *Chem. Rev.* **2019**, *119* (12), 7610−7672.
(16) Reller, C.; Krause, R.; Volkova, E.; Schmid, B.; Neubauer, S.; Rucki, A.; Schuster, M.; Schmid, G. Selective Electroreduction of $CO_2$ toward Ethylene on Nano Dendritic Copper Catalysts at High Current Density. *Adv. Energy Mater.* **2017**, *7* (12), 1602114.
(17) Albo, J.; Irabien, A. $Cu_2O$-Loaded Gas Diffusion Electrodes for the Continuous Electrochemical Reduction of $CO_2$ to Methanol. *J. Catal.* **2016**, *343*, 232−239.
(18) Zhao, Y.; Chang, X.; Malkani, A. S.; Yang, X.; Thompson, L.; Jiao, F.; Xu, B. Speciation of Cu Surfaces during the Electrochemical CO Reduction Reaction. *J. Am. Chem. Soc.* **2020**, *142* (21), 9735−9743.
(19) Grosse, P.; Yoon, A.; Rettenmaier, C.; Herzog, A.; Chee, S. W.; Roldan Cuenya, B. Dynamic Transformation of Cubic Copper Catalysts during $CO_2$ Electroreduction and Its Impact on Catalytic Selectivity. *Nat. Commun.* **2021**, *12* (1), 6736.
(20) Simon, G. H.; Kley, C. S.; Roldan Cuenya, B. Potential-Dependent Morphology of Copper Catalysts During $CO_2$ Electroreduction Revealed by In Situ Atomic Force Microscopy. *Angew. Chem., Int. Ed.* **2021**, *60* (5), 2561−2568.
(21) Phan, T. H.; Banjac, K.; Cometto, F. P.; Dattila, F.; García-Muelas, R.; Raaijman, S. J.; Ye, C.; Koper, M. T. M.; López, N.; Lingenfelder, M. Emergence of Potential-Controlled Cu-Nanocuboids and Graphene-Covered Cu-Nanocuboids under Operando $CO_2$ Electroreduction. *Nano Lett.* **2021**, *21* (5), 2059−2065.
(22) Osowiecki, W. T.; Nussbaum, J. J.; Kamat, G. A.; Katsoukis, G.; Ledendecker, M.; Frei, H.; Bell, A. T.; Alivisatos, A. P. Factors and Dynamics of Cu Nanocrystal Reconstruction under $CO_2$ Reduction. *ACS Appl. Energy Mater.* **2019**, *2* (11), 7744−7749.
(23) Yanson, A. I.; Rodriguez, P.; Garcia-Araez, N.; Mom, R. V.; Tichelaar, F. D.; Koper, M. T. M. Cathodic Corrosion: A Quick, Clean, and Versatile Method for the Synthesis of Metallic Nanoparticles. *Angew. Chem., Int. Ed.* **2011**, *50* (28), 6346−6350.
(24) Popovic, S.; Bele, M.; Hodnik, N. Reconstruction of Copper Nanoparticles at Electrochemical $CO_2$ Reduction Reaction Conditions Occurs via Two-step Dissolution/Redeposition Mechanism. *ChemElectroChem* **2021**, *8* (14), 2634−2639.
(25) Raaijman, S. J.; Arulmozhi, N.; Koper, M. T. M. Morphological Stability of Copper Surfaces under Reducing Conditions. *ACS Appl. Mater. Interfaces* **2021**, *13* (41), 48730−48744.
(26) Speck, F. D.; Cherevko, S. Electrochemical Copper Dissolution: A Benchmark for Stable $CO_2$ Reduction on Copper Electrocatalysts. *Electrochem. Commun.* **2020**, *115*, 106739.
(27) Velasco-Velez, J.-J.; Mom, R. V.; Sandoval-Diaz, L.-E.; Falling, L. J.; Chuang, C.-H.; Gao, D.; Jones, T. E.; Zhu, Q.; Arrigo, R.; Roldan Cuenya, B.; Knop-Gericke, A.; Lunkenbein, T.; Schlögl, R. Revealing the Active Phase of Copper during the Electroreduction of $CO_2$ in Aqueous Electrolyte by Correlating In Situ X-Ray Spectroscopy and In Situ Electron Microscopy. *ACS Energy Lett.* **2020**, *5* (6), 2106−2111.
(28) Kas, R.; Kortlever, R.; Milbrat, A.; Koper, M. T. M.; Mul, G.; Baltrusaitis, J. Electrochemical $CO_2$ Reduction on $Cu_2O$-Derived Copper Nanoparticles: Controlling the Catalytic Selectivity of Hydrocarbons. *Phys. Chem. Chem. Phys.* **2014**, *16* (24), 12194−12201.
(29) Li, Y.; Cui, F.; Ross, M. B.; Kim, D.; Sun, Y.; Yang, P. Structure-Sensitive $CO_2$ Electroreduction to Hydrocarbons on Ultrathin 5-Fold Twinned Copper Nanowires. *Nano Lett.* **2017**, *17* (2), 1312−1317.
(30) Loiudice, A.; Lobaccaro, P.; Kamali, E. A.; Thao, T.; Huang, B. H.; Ager, J. W.; Buonsanti, R. Tailoring Copper Nanocrystals towards $C_2$ Products in Electrochemical $CO_2$ Reduction. *Angew. Chem., Int. Ed.* **2016**, *55* (19), 5789−5792.
(31) Qiu, Y.-L.; Zhong, H.-X.; Zhang, T.-T.; Xu, W.-B.; Li, X.-F.; Zhang, H.-M. Copper Electrode Fabricated via Pulse Electrodeposition: Toward High Methane Selectivity and Activity for $CO_2$ Electroreduction. *ACS Catal.* **2017**, *7* (9), 6302−6310.
(32) Jia, Y.; Li, F.; Fan, K.; Sun, L. Cu-Based Bimetallic Electrocatalysts for $CO_2$ Reduction. *Adv. Powder Mater.* **2022**, *1* (1), 100012.
(33) Ismail, A. M.; Samu, G. F.; Balog, Á.; Csapó, E.; Janáky, C. Composition-Dependent Electrocatalytic Behavior of Au−Sn Bimetallic Nanoparticles in Carbon Dioxide Reduction. *ACS Energy Lett.* **2019**, *4* (1), 48−53.
(34) Sassenburg, M.; Iglesias van Montfort, H. P.; Kolobov, N.; Smith, W. A.; Burdyny, T. Bulk Layering Effects of Ag and Cu for Tandem $CO_2$ Electrolysis. *ChemSusChem* **2025**, *18* (8), No. e202401769.
(35) Reske, R.; Mistry, H.; Behafarid, F.; Roldan Cuenya, B.; Strasser, P. Particle Size Effects in the Catalytic Electroreduction of $CO_2$ on Cu Nanoparticles. *J. Am. Chem. Soc.* **2014**, *136* (19), 6978−6986.
(36) Manthiram, K.; Beberwyck, B. J.; Alivisatos, A. P. Enhanced Electrochemical Methanation of Carbon Dioxide with a Dispersible Nanoscale Copper Catalyst. *J. Am. Chem. Soc.* **2014**, *136* (38), 13319−13325.
(37) De Gregorio, G. L.; Burdyny, T.; Loiudice, A.; Iyengar, P.; Smith, W. A.; Buonsanti, R. Facet-Dependent Selectivity of Cu Catalysts in Electrochemical $CO_2$ Reduction at Commercially Viable Current Densities. *ACS Catal.* **2020**, *10* (9), 4854−4862.


https://doi.org/10.1021/acsaem.5c01142
ACS Appl. Energy Mater. 2025, 8, 8551−8560

(38) Kim, D.; Kley, C. S.; Li, Y.; Yang, P. Copper Nanoparticle Ensembles for Selective Electroreduction of CO2 to $C_2$−$C_3$ Products. *Proc. Natl. Acad. Sci. U.S.A.* **2017**, *114* (40), 10560−10565.
(39) Merino-Garcia, I.; Albo, J.; Irabien, A. Tailoring Gas-Phase $CO_2$ Electroreduction Selectivity to Hydrocarbons at Cu Nanoparticles. *Nanotechnology* **2018**, *29* (1), 014001.
(40) Wang, Z.; Yang, G.; Zhang, Z.; Jin, M.; Yin, Y. Selectivity on Etching: Creation of High-Energy Facets on Copper Nanocrystals for $CO_2$ Electrochemical Reduction. *ACS Nano* **2016**, *10* (4), 4559−4564.
(41) Burdyny, T.; Smith, W. A. $CO_2$ Reduction on Gas-Diffusion Electrodes and Why Catalytic Performance Must Be Assessed at Commercially-Relevant Conditions. *Energy Environ. Sci.* **2019**, *12* (5), 1442−1453.
(42) Endrődi, B.; Bencsik, G.; Darvas, F.; Jones, R.; Rajeshwar, K.; Janáky, C. Continuous-Flow Electroreduction of Carbon Dioxide. *Prog. Energy Combust. Sci.* **2017**, *62*, 133−154.
(43) García de Arquer, F. P.; Dinh, C. T.; Ozden, A.; Wicks, J.; McCallum, C.; Kirmani, A. R.; Nam, D. H.; Gabardo, C.; Seifitokaldani, A.; Wang, X.; Li, Y. C.; Li, F.; Edwards, J.; Richter, L. J.; Thorpe, S. J.; Sinton, D.; Sargent, E. H. $CO_2$ Electrolysis to Multicarbon Products at Activities Greater than 1 A $Cm^{-2}$. *Science* **2020**, *367* (6478), 661−666.
(44) Dinh, C.-T.; Burdyny, T.; Kibria, M. G.; Seifitokaldani, A.; Gabardo, C. M.; García de Arquer, F. P.; Kiani, A.; Edwards, J. P.; De Luna, P.; Bushuyev, O. S.; Zou, C.; Quintero-Bermudez, R.; Pang, Y.; Sinton, D.; Sargent, E. H. $CO_2$ Electroreduction to Ethylene via Hydroxide-Mediated Copper Catalysis at an Abrupt Interface. *Science* **2018**, *360* (6390), 783−787.
(45) Ma, S.; Sadakiyo, M.; Luo, R.; Heima, M.; Yamauchi, M.; Kenis, P. J. A. One-Step Electrosynthesis of Ethylene and Ethanol from $CO_2$ in an Alkaline Electrolyzer. *J. Power Sources* **2016**, *301*, 219−228.
(46) Ma, M.; Clark, E. L.; Therkildsen, K. T.; Dalsgaard, S.; Chorkendorff, I.; Seger, B. Insights into the Carbon Balance for $CO_2$ Electroreduction on Cu Using Gas Diffusion Electrode Reactor Designs. *Energy Environ. Sci.* **2020**, *13* (3), 977−985.
(47) Chen, L.; Chen, J.; Fan, L.; Chen, J.; Zhang, T.; Chen, J.; Xi, S.; Chen, B.; Wang, L. Additive-Assisted Electrodeposition of Cu on Gas Diffusion Electrodes Enables Selective $CO_2$ Reduction to Multicarbon Products. *ACS Catal.* **2023**, *13* (18), 11934−11944.
(48) Serfőző, A.; Csík, G. A.; Kormányos, A.; Balog, A.; Janáky, C.; Endrődi, B. One-Step Electrodeposition of Binder-Containing Cu Nanocube Catalyst Layers for Carbon Dioxide Reduction. *Nanoscale* **2023**, *15* (41), 16734−16740.
(49) Hoang, T. T. H.; Ma, S.; Gold, J. I.; Kenis, P. J. A.; Gewirth, A. A. Nanoporous Copper Films by Additive-Controlled Electrodeposition: $CO_2$ Reduction Catalysis. *ACS Catal.* **2017**, *7* (5), 3313−3321.
(50) Hoang, T. T. H.; Verma, S.; Ma, S.; Fister, T. T.; Timoshenko, J.; Frenkel, A. I.; Kenis, P. J. A.; Gewirth, A. A. Nanoporous Copper−Silver Alloys by Additive-Controlled Electrodeposition for the Selective Electroreduction of $CO_2$ to Ethylene and Ethanol. *J. Am. Chem. Soc.* **2018**, *140* (17), 5791−5797.
(51) Li, J.; Ma, L.; Li, X.; Lu, C.; Liu, H. Effect of Nitric Acid Pretreatment on the Properties of Activated Carbon and Supported Palladium Catalysts. *Ind. Eng. Chem. Res.* **2005**, *44* (15), 5478−5482.
(52) Pacquets, L.; Irtem, E.; Neukermans, S.; Daems, N.; Bals, S.; Breugelmans, T. Size-Controlled Electrodeposition of Cu Nanoparticles on Gas Diffusion Electrodes in Methanesulfonic Acid Solution. *J. Appl. Electrochem.* **2021**, *51* (2), 317−330.
(53) Zhang, Y.; Cai, Z.; Zhao, Y.; Wen, X.; Xu, W.; Zhong, Y.; Bai, L.; Liu, W.; Zhang, Y.; Zhang, Y.; Kuang, Y.; Sun, X. Superaerophilic Copper Nanowires for Efficient and Switchable $CO_2$ Electroreduction. *Nanoscale Horiz.* **2019**, *4* (2), 490−494.
(54) Gabardo, C. M.; O'Brien, C. P.; Edwards, J. P.; McCallum, C.; Xu, Y.; Dinh, C.-T.; Li, J.; Sargent, E. H.; Sinton, D. Continuous Carbon Dioxide Electroreduction to Concentrated Multi-Carbon Products Using a Membrane Electrode Assembly. *Joule* **2019**, *3* (11), 2777−2791.
(55) Ross, B.; Haussener, S.; Brinkert, K. Impact of Gas Bubble Evolution Dynamics on Electrochemical Reaction Overpotentials in Water Electrolyser Systems. *J. Phys. Chem. C* **2025**, *129*, 4383−4397.
(56) Zaza, L.; Rossi, K.; Buonsanti, R. Well-Defined Copper-Based Nanocatalysts for Selective Electrochemical Reduction of $CO_2$ to $C_2$ Products. *ACS Energy Lett.* **2022**, *7*, 1284−1291.
(57) Huang, J.; Hörmann, N.; Oveisi, E.; Loiudice, A.; De Gregorio, G. L.; Andreussi, O.; Marzari, N.; Buonsanti, R. Potential-Induced Nanoclustering of Metallic Catalysts during Electrochemical $CO_2$ Reduction. *Nat. Commun.* **2018**, *9* (1), 1−9.


https://doi.org/10.1021/acsaem.5c01142
ACS Appl. Energy Mater. 2025, 8, 8551−8560